Journal of The Electrochemical Society, 2023 **170** 070516

Assessing Electrolyte Fluorination Impact on Calendar Aging of Blended Silicon-Graphite Lithium-Ion Cells Using Potentiostatic Holds

Ankit Verma,[1,*,z] Maxwell C. Schulze,[1] Andrew Colclasure,[1] Marco-Tulio Fonseca Rodrigues,[2] Stephen E Trask,[2] Krzysztof Pupek,[3] Christopher S. Johnson,[2,] and Daniel P. Abraham[2,*]**

[1]*Energy Conversion and Storage Systems Center, National Renewable Energy Laboratory, Golden, Colorado, United States of America*
[2]*Chemical Sciences and Engineering Division, Argonne National Laboratory, Lemont, Illinois 60439, United States of America*
[3]*Applied Materials Division, Argonne National Laboratory, Lemont, Illinois 60439, United States of America*

Silicon-based lithium-ion batteries have started to meet cycle life metrics, but they exhibit poor calendar life. Here, electrolyte fluorination impact on calendar fade of blended silicon-graphite anodes is explored using a $LiPF_6$ in EC:EMC:FEC electrolyte vs LiBOB in EC:EMC electrolyte. We utilize a combined experimental-modeling approach applying potentiostatic voltage holds (V-hold) to evaluate electrolyte suitability for calendar life in a shortened testing timeframe (~2 months). Our theoretical framework deconvolutes the irreversible parasitic capacity losses (lithium lost to the solid electrolyte interphase) from the V-hold electrochemical data. Unfluorinated electrolyte (dominant LiBOB reduction) exhibits higher cell resistance as compared to fluorinated electrolyte (dominant FEC reduction). Both systems have similar irreversible capacities during the voltage hold duration with slower rate of parasitic capacity loss for the LiBOB system. Extrapolation of the parasitic losses to end of life capacity fade of 20% shows LiBOB electrolyte outperforming $LiPF_6$ electrolyte in calendar life. The results demonstrate the applicability of the V-hold protocol as a rapid material screening tool providing semi-quantitative calendar lifetime estimates.
 [DOI: 10.1149/1945-7111/ace65d]

Manuscript submitted April 28, 2023; revised manuscript received July 3, 2023. Published July 19, 2023.

Supplementary material for this article is available online

Lithium-ion battery (LIB) technology has become the ubiquitous energy storage device for portable electronics, with fast inroads being made towards grid storage and mobility applications.[1–4] Rising demands of energy storage can be met by high energy, power density cells enabled by novel cathode and anode materials. State-of-the-art cathode candidates comprise high voltage, nickel-rich nickel-manganese-cobalt oxide (NMC) family of materials offering high energy densities and specific capacities reaching 200 mAh g_{NMC}^{-1}.[5,6] Paired with graphite (Gr) anodes, they have achieved cell level metrics surpassing 250 Wh kg^{-1}, showcasing cycle and calendar lifetimes exceeding 1000 cycles and 15 years, respectively.[7] The next step change in cell energy densities (350–500 Wh kg^{-1}) will be afforded by substituting the graphite anode with silicon (Si) or lithium (Li) metal.[8,9] The theoretical gravimetric capacities of Si and Li metal can reach 4200 mAh g_{Si}^{-1} and 3860 mAh g_{Li}^{-1}, surpassing graphite's theoretical capacity of 372 mAh g^{-1} nearly tenfold. Si–Gr blends provide a pathway for incremental progress towards the 350 Wh kg^{-1} metric without introducing huge challenges associated with completely swapping the stable Gr chemistry for Si. In fact, commercial cell manufacturers have steadily increased the energy densities by incorporating up to 10 wt% silicon with graphite in the anode.[10–12]

In the literature, cycling of silicon anodes has been researched extensively with the primary aim of mitigating the consequences of the ~300% volumetric change of Si with lithiation/delithiation. These cyclic changes can lead to fracture and decrepitation of the silicon active material as well as continuous formation of the passivating solid electrolyte interphase (SEI) film.[13–16] Nano-sized silicon (nanospheres/nanowires),[17,18] core shell architectures,[19] electrolyte additives,[20,21] and elastomeric artificial SEI layers[22] strategies are utilized to stabilize the silicon + SEI agglomerate and have been reasonably successful in extending the cycle life to graphite levels.[23] However, the calendar life (time-dependent capacity loss, resistance rise on storage at open circuit conditions without cycling) of silicon-based LIBs is a much less researched topic in the literature as compared to graphite-based LIBs.[24–30] McBrayer et al. highlighted the substantial gap between the calendar life of silicon (maximum 20 months) vs graphite (exceeding 120 months) cells from leading manufacturers.[23] High (electro)chemical reactivity of the silicon anode chemistry is thought to form a non-passivating SEI that allows for continued deleterious solvent/salt decomposition even at open circuit conditions, resulting in rapid loss of lithium inventory (LLI) and drastically lowered calendar lifetimes.[23]

Traditionally, calendar life testing is performed using the United States Advanced Battery Consortium's open circuit voltage—reference performance test (USABC OCV-RPT) protocol, requiring years-long testing to generate sufficient experimental data for quantitative prediction of calendar life.[31] Naumann et al. have run calendar aging studies on LFP-graphite cells for 29 months (>2 years) where the cell capacities were still above 80%.[32] Rodrigues et al. have aged Si-Gr pouch cells over for 4 years.[33] Calendar life of Si containing cells manufactured by companies have reached 20 months.[23] Repeated capacity, resistance checks at ~30 day intervals between OCV rests with optional daily pulses to maintain the constant potential form the crux of the protocol; subsequently, statistical regression analysis/machine learning on the capacity, resistance data vs time provide equation fits that can be extrapolated to provide lifetime estimates for when the cell reaches a predefined fraction, generally 80%, of its pristine capacity.[34] Recently, potentiostatic-hold protocols have been explored for rapid battery calendar life screening to obviate the needs for years-long testing.[35] This provides an avenue for rapid material screening for Si calendar life. In this article, we utilize this voltage-hold (V-hold) protocol to analyze the impact of electrolyte fluorination on calendar lifetime of blended 15% Si−73% graphite anode|NMC532 cathode batteries. The V-hold protocol has signatures from reversible as well as

*Electrochemical Society Member.
**Electrochemical Society Fellow.
[z]E-mail: ankit.verma@nrel.gov

irreversible capacity that is exchanged during the hold; this article devises a deconvolution algorithm to estimate the irreversible proportion and extrapolate the estimates to predict semi-quantitative calendar lifetime of the cell. This numerical approach is especially important for Si cells, as this material has been shown to exhibit slow reversible relaxation that could affect the interpretation of V-hold experiments.[35] The combined experiment-modeling approach provides a pathway towards rapid (<2 months test duration) screening of electrode and electrolyte materials for calendar life.

The rest of the article is divided as follows. Details of the experimental methods including materials, cell design and electrochemical testing protocol are elaborated first. Then, the theoretical foundations for extraction of parasitic SEI capacity losses from V-hold data are established. Electrochemical data from fluorinated vs unfluorinated system is analyzed using this framework to delineate the dominant electrolyte reduction mechanism, impedance effects, and deconvoluted reversible, irreversible capacities which is subsequently extrapolated to compare calendar lifetimes of these cells. Additional data to support our analysis are presented in the Supporting Information which is referenced in the text with the designator "S".

Experiments: Materials, Cell Design and Electrochemical Testing

The positive and negative electrode sheets were fabricated at the Cell Analysis, Modeling and Prototyping (CAMP) facility at Argonne National Laboratory. Table S1 in the Supporting Information lists the electrode and electrolyte materials; Fig. S1a delineates the chemical formula and structure of the electrolyte salt and solvent constituents used in this study The anode comprises 15 wt% NanoAmor silicon nanoparticles (50–70 nm) with 73 wt% Hitachi MAGE Graphite (>20 μm), C45 (Timcal) carbon conductive additive for enhanced electron transport and lithium-exchanged polyacrylic acid (LiPAA) binder to hold the constituents together. The cathode is Ni rich NMC532 active material, C45 carbon conductive additive and polyvinylidene fluoride (PVdF). The anode was dried at 150 °C, the cathode at 120 °C and the microporous polymer separators were dried at 75 °C in a vacuum oven.

Two electrolyte systems were prepared to distinguish the impact of electrolyte fluorination on calendar life. The fluorinated electrolyte comprised of 1.2 M lithium hexafluorophosphate ($LiPF_6$) salt in a 3:7 w/w liquid mixture of ethylene carbonate (EC) and ethyl methyl carbonate (EMC) to which 10 wt% fluoroethylene carbonate (FEC) is added for SEI stabilization. In the absence of FEC, high dielectric constant cyclic carbonate EC ($\varepsilon = 90$) solvates the Li^+ ion forming the "good" SEI decomposition products while the low viscosity linear carbonate EMC ($\varepsilon = 3.1$) provides enhanced mobility.[36–40] Cyclic carbonate FEC ($\varepsilon = 105$) additive revamps the diluent structure with a more dominant presence in the Li^+ solvation shell compared to EC, EMC.[41,42] Furthermore, it preferentially decomposes to form electron insulating lithium fluoride and vinylene carbonate (VC) that can polymerize to form cross-linked poly(VC) with elastomeric properties enabling a passivating, mechanically flexible SEI film.[43–47] However, fluorinated electrolytes can also decompose to form toxic, corrosive compounds like hydrofluoric acid which can etch away the electrode materials leading to capacity deterioration.[48–50] In contrast, the unfluorinated electrolyte system consists of environmentally benign 0.7 M lithium bis(oxalato)borate (LiBOB) salt in a 3:7 w/w EC:EMC. Previously, Kang Xu and collaborators have explored the beneficial characteristics of LiBOB based electrolyte with respect to graphite anodes where it can effectively prevent the exfoliation of graphitic anodes in propylene carbonate (PC) solvent while $LiPF_6$ in pure PC electrolyte destroys the graphite anode.[51–57] The participation of BOB anion in SEI formation alongside EC decomposition leads to passivating surface film formation consisting of lithium oxalates and borates on both anode and cathode, enhancing the cell performance at high voltages and temperatures.[58–61]

Electrochemical cells comprising of Si–Gr anode, NMC532 cathode and fluorinated/unfluorinated electrolyte were assembled under argon (Ar) atmosphere in a glovebox. Cells were equipped with a Li/Cu reference electrode (see Fig. S1b for cell schematic) to enable individual tracking of anode and cathode potentials vs Li/Li^+ alongside the cell voltage. Each cell contained 20.3 cm^2 electrodes separated by two Celgard 2325 separators and a 25 μm reference wire. Electrochemical cycling and V-hold of the cells was performed using a Maccor Model 2300 battery system at 30 °C. The electrochemical protocol consisted of three constant current (CC) formation cycles at C/20 rate followed by a constant current constant voltage (CCCV) hold cycle and ends with two additional diagnostic CC cycles at C/20 rate resulting in a total of six cycles. During all cycling, the cell voltage varies between 3.0 V and 4.1 V. The 4th cycle is the V-hold cycle consisting of a C/20 charge up to 4.1 V followed by a maximum of 600 h V-hold at the top of charge and subsequent discharge to 3.0 V.

Cell impedance was evaluated after formation by electrochemical impedance spectroscopy (EIS) and hybrid pulse power characterization (HPPC) tests. HPPC protocol consists of a 10 s 3C discharge and corresponding 10 s 2.25C charge pulse separated by 40 s open circuit following a 1 h rest. The HPPC pulses, which are electrochemical protocols to determine cell power losses, were measured during cell discharge at voltage intervals after charging the cell to 4.1 V. AC impedance spectra were obtained between 100 kHz to 10 mHz with 10 measurements per decade and a 5 mV rms potential perturbation from open circuit. EIS was run at 3.7 V full cell voltage. This corresponds to nearly 50% SOC. Cycling and HPPC tests were performed using a Maccor Model 2300 battery test system and EIS measurements using a Solartron Analytical 1470E cell test system. Instrument specifications are given in Table I.

Deconvolution of Parasitic Capacity from Voltage Hold Cycle

Figure 1 shows (a) voltage vs time for the entire V-hold cycle and (b) capacity and current during the 600 h 4.1 V hold for the fluorinated electrolyte. The nominal capacity of the cell is 27.78 mAh while 2.31 mAh capacity is exchanged during the 600 h hold. The current during the hold lies in the 10^{-2} to 10^{-4} mA range indicating extremely low currents for the latter half of the hold time. The capacity exchanged before the V-hold (Q_1), during the V-hold (Q_{hold}), and after the V-hold (Q_2) is required to be analyzed for fade requiring accurate deconvolution of reversible (lithiation behavior) vs irreversible (solid electrolyte interphase behavior) currents during the V-hold. While the reversible currents arise from continued anode lithiation (cathode delithiation) at constant cell voltage (after the constant current

Table I. Electrochemical measurement instrument specifications.

Instrument	Max current in range	Current accuracy	Current resolution	Voltage accuracy	Voltage resolution
Maccor Series 2300	150 μA	30 nA	2.3 nA	2 mV	150 μV
	5 mA	1 μA	76.3 nA		
	150 mA	30 μA	2.3 μA		
	5000 mA	1 mA	76.3 μA		
Solartron 1470E	50 μA	25 nA	1.5 nA	1 mV	3 μV

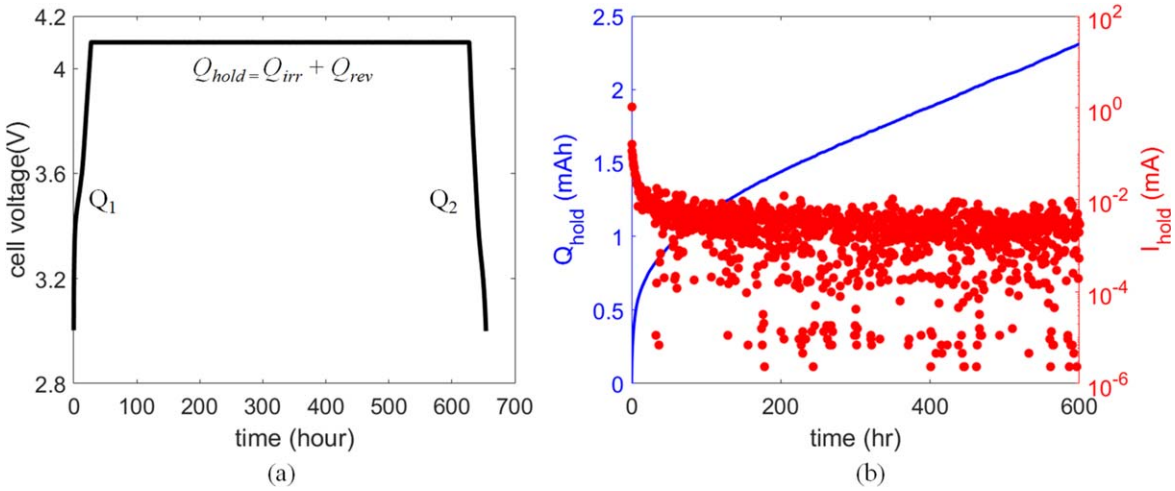

Figure 1. (a) Cell voltage (in volts) vs time (in hours) for the voltage-hold cycle, (b) Capacity (in mAh) and current (in mA) vs time for the constant voltage part of the voltage-hold cycle for the fluorinated electrolyte.

portion), irreversible currents can arise from electrochemical parasitic side-reactions occurring during the V-hold leading to loss of lithium inventory (LLI) through SEI growth.

Silicon anodes showcase long reversible lithiation timescales. Inverse polarization experiments have been run to estimate that reversible lithiation can run for hundreds of hours for 80% Si anodes.[35] Consequently, we chose 600 h as the duration of the voltage hold so that we get data for reversible as well as irreversible capacity changes. During the constant current charging step, data was logged at every 5 mV change or 900 s, whichever was lower. During the constant voltage step, data was logged at every 30 min (1800 s). Current during the latter half of the voltage hold lies between 0.5 to 5 μA. In Schulze et al. (see Section S6 of SI), we have shown that current noise is not always related to poor hardware accuracy.[35] It also gives a few examples of cases in which there are different levels of noise but end up having the same progression of the integrated capacity.

Fits are performed on the capacity data as it does not show the stochasticity of the current data and is a monotonically increasing function. The apparent stochasticity of the current data is due to the nature of conducting voltage hold with Maccor cyclers. In the constant current step, the cycler maintains a constant C/20 current specified by the user. In the voltage-hold step, the cycler must maintain a constant voltage and provides a decreasing current to stabilize the voltage. Maccor cyclers can only provide positive or zero current during the voltage hold step. At a particular instant the cycler calculates a particular current to reach the constant upper voltage cutoff. If the voltage exceeds the cutoff, in the next step the current is closer to 0 to drop the voltage. So, we see the cycler current appears stochastic as it is not a fixed value and is adjusted accordingly to maintain the same voltage.

Quantification of the irreversible capacity portion during the V-hold for anodes containing silicon is further complicated by zero-current voltage and capacity hysteresis observed for silicon.[62,63] Phase-transformation, particle-size distribution related geometric effects and large magnitude stresses in large deformation Si particles (300% expansion) can cause hysteresis (voltage gap) in the open circuit potentials between lithiation and delithiation of the Si anode.[64,65] This hysteresis is exacerbated during finite rate (CC) battery operation as stress buildup in the Si particle and electrode can further impact alloying reaction kinetics at the interface and solid-state Li transport in the Si particle.[66] Thus, with an increase in Si weight proportions in GrlSi anode compositions, there is an increase in hysteresis gap which necessitates proper accounting. Pure graphite-based lithium-ion battery systems can show nearly 100% energy efficiency at slow current rates (e.g. C/20) with minimal gap in the equilibrium potential between lithiation and delithiation in the absence of parasitic SEI losses. This is due to much smaller strains (10% volumetric expansion) in the system leading to nearly full thermodynamic reversibility in the absence of diffusive transport and electrochemical kinetics related losses at slow rates.[67] For Si anode, the thermodynamic reversibility is not achieved because of the wide variation in surface stress states (compressive to tensile with magnitudes of the order of gigapascals) between lithiation and delithiation from finite strain effects which can heavily impact the reaction kinetics as well as Li diffusive transport.[68–70] Interestingly, experimental data suggests that Si shows nearly an order of magnitude higher lithiation diffusivity (charge) as compared to delithiation (discharge),[71] and charge transfer kinetic magnitudes can double from delithiation to lithiation.[72] Furthermore, Li diffusivity in Si can be two to four orders of magnitudes slower in silicon (10^{-16} to 10^{-18} $m^2\,s^{-1}$)[71,72] as compared to graphite ($10^{-14}\,m^2\,s^{-1}$).[73] Hence, the observed electrochemical signatures of Si anodes can show gaps in equilibrium potential and measured capacity between lithiation and delithiation even at slow rate cycling. Consequently, we devise a parasitic capacity estimation technique that account for hysteresis in graphite-Si blends in addition to understanding the reversible lithiation of Si that happens during the V-hold.

During the CV-hold after the CC stage, there is further lithiation of the Si–Gr blend with decreasing current magnitudes. The continued lithiation of Si–Gr anode contributes to reversible capacity portion (can ideally be extracted during delithiation) of the V-hold, hence termed Q_{rev}. Furthermore, parasitic SEI reactions occur at the Si–Gr blended anode from solvent and salt decomposition pathways during the V-hold and can result in irreversible capacity loss, Q_{irrev}. EC reductive decomposition to organic Li_2EDC has been proposed in the literature below 0.8 V, with further decomposition to inorganic carbonates and oxides around 0.3 V (vs Li) for the anode potential respectively.[74–77] FEC decomposition to LiF and VC is also proposed below 0.9 V.[78–80] Salt decomposition pathways in the absence of water is not clearly understood and water catalyzed hydrolysis reactions have been proposed to cause $LiPF_6$ decomposition to LiF.[81,82] Consequently, the capacity measured during V-hold is a sum of irreversible SEI growth and reversible Si–Gr lithiation.

Irreversible capacity losses during calendar aging typically show a power law nature with time, and $Q_{irr} = at^p$ has been proposed to estimate the irreversible capacity lost to SEI growth.[83] The exponent p can take values ranging from 0.2–1, depending on early, intermediate, and long-term SEI growth regimes. Several physics-based SEI growth mechanisms have been proposed in the literature, including electron conduction, electron tunneling, interstitial Li

transport and solvent transport, and show a square root of time growth dependence of SEI thickness.[84,85] Larger exponents > 0.5 can stem from the creation of new particle surfaces due to particle cracking which can be attacked by the electrolyte leading to fresh SEI formation. Smaller exponents < 0.5 can be attributed to dissolution of solid phase decomposition products of the SEI back into the electrolyte or conversion of high molar volume SEI components like Li_2EDC, Li_2CO_3 to low molar volume inorganic products like Li_2O, resulting in a decrease in SEI thickness.[86] The phenomena of SEI breathing during cycling has been well documented in Si literature; $LiPF_6$ in EC:EMC electrolyte causes SEI growth during lithiation and dissolution during delithiation while the opposite is observed with the addition of 10% FEC to the electrolyte.[87–89]

The estimation of the irreversible capacity loss is described in detail here. Let Q_1, Q_2 and Q_{hold} be the capacity exchanged before, after and during the V-hold respectively. The capacity during the V-hold can be represented as the sum of irreversible, Q_{irr} and reversible contributions, Q_{rev}:

$$Q_{hold}\ (t) = Q_{irr}(t) + Q_{rev}(t) = at^p + \frac{Q_{rev}^{final}(c + t_{final})t}{t_{final}(c + t)} \quad [1]$$

$$Q_{hold}^{final} = Q_{irrev}^{final} + Q_{rev}^{final} \quad [2]$$

Hold current is obtained from the capacity model fit through:

$$i_{hold}(t) = \frac{dQ_{hold}(t)}{dt} = pat^{p-1} + \frac{Q_{rev}^{final}(c + t_{final})c}{t_{final}(c + t)^2} \quad [3]$$

While Q_{irr} shows the power law dependence on time, the form of reversible capacity, Q_{rev}, is chosen to replicate the plateauing behavior of reversible lithiation of Si-Gr blend as the V-hold time increases. Note S1 provides a list of heuristic equation choices for reversible capacity. $\frac{Q_{rev}^{final}(c + t_{final})t}{t_{final}(c + t)}$ expression for reversible capacity gives the highest goodness of fit and lowest residuals for hold capacity (see Figs. S2–S5) when fitting Eqs. 1–2. A derivation of the exact form of Eq. 1 is presented in Note S2. Here, Q_{hold}^{final}, Q_{irr}^{final}, Q_{rev}^{final} are the cumulative hold, irreversible, and reversible capacities exchanged by the end of V-hold time duration, t_{final}, respectively. The parameter c (in the reversible capacity formula) with units of time is physically relevant; it is a measure of reversible lithiation rate of Si-Gr blends during the constant V-hold. A small magnitude of c indicates fast relaxation of transport and kinetic processes throughout the Si–Gr blended anode particles allowing for rapid anode lithiation to its final reversible capacity Q_{rev}^{final} during early times of the hold. In contrast, a high value of the c parameter indicates that the CV lithiation of Si–Gr blend is a slow process (high impedance, slow transport), allowing for reversible lithiation to occur for a longer portion of the V-hold before approaching its final value. It is evident that there are four unknown parameters, a, p, Q_{rev}^{final} and c to be estimated for an accurate deconvolution of the V-hold capacity data and subsequent estimation of the calendar lifetime. For an assumed value of $p = 0.5$ obtained from physics-based models of SEI growth, the number of unknowns decrease to 3: a, Q_{rev}^{final} and c. A deeper dive into the physical significance of the fit parameters is presented in Note S3, with impact of variation of the fit parameters on the temporal trends of normalized capacity shown in Fig. S6.

The capacities before and after the V-hold can be correlated to the reversible lithiation and irreversible parasitic capacity components during V-hold and the apparent capacity loss related to hysteresis, Q_{hys}. The anode is getting lithiated during CC as well as the CV portions. During the subsequent delithiation, there will be a slight loss in capacity from the hysteresis impact which combines OCV gap, impedance rise of the cell and any rate limitations that can arise from C/20 cycling for silicon. Note that C/20 is very slow current rate cycling, and for a typical commercial graphite-NMC system the hysteresis capacity, Q_{hys}, obtained will be negligible. As the Si content of the anode increases, an increase in Q_{hys} is expected to be observed. For a half cell (N:P $\gg$ 1), or cell with an oversized cathode (N:P $\ll$ 1) with flat cathode voltage profile,[35] an excess of Li inventory is present. Any loss in lithium inventory due to the parasitic reactions will be covered by the surplus of Li present and hence the anode delithiation capacity after V-hold is not impacted by the irreversible Li loss to the SEI:

$$Q_{rev}^{final} = Q_2 - Q_1 + Q_{hys} \quad [4]$$

For a full cell, the cell becomes nearly perfectly balanced after the formation cycling leading to a N:P ratio of 1. Any subsequent loss of Li to SEI during the V-hold will impact the delithiation capacities after the V-hold:

$$Q_2 = Q_1 + Q_{rev}^{final} - Q_{irrev}^{final} - Q_{hys} \quad [5]$$

Note that the additional capacity gained in discharge through the reservoir effect[90] is ignored here. Combined with Eq. 2, for the full NMC532|Si-Gr cell being held at 4.1 V this gives:

$$Q_{rev}^{final} = (Q_{hold}^{final} + Q_{hys} + Q_2 - Q_1)/2.0 \quad [6]$$

Finally, the irreversible portion can be estimated for both half and full cells by:

$$Q_{irrev}^{final} = Q_{hold}^{final} - Q_{rev}^{final} = at_{final}^{p} \quad [7]$$

It is evident that quantification of the unknown Q_{hys} from experimental data is integral to accurate estimation of the irreversible capacity during the V-hold. Q_{hys} is computed to a first approximation from the difference in the charge and discharge capacities of the C/20 cycling data after the V-hold cycle, noting that a portion of the difference in capacities at slow C/20 current rates should stem from the combined hysteresis effect. We estimate Q_{hys} through the fit defining an upper bound for it from the difference in charge and discharge capacities in the cycle after the hold. The combined 40 h of anode lithiation during cycles 5 and 6 will also have contributions from SEI irreversible capacity loss, but since the anode voltage cycles between ~0.1 V and 0.7 V, the driving force for SEI formation during cycling is relatively meager as compared to V-hold where the anode potentials lie close to 0.1 V throughout the entire 600 h duration. Consequently, irreversible SEI losses during full cell C/20 cycling after V-hold cycle is assumed to be negligible and the capacity difference between charge and discharge can be attributed to max value of hysteresis. Furthermore, loss of active material related capacity loss is neglected since the experimental protocol consists of few, slow C/20 cycles on nanosized Si (~50–70 nm) below the critical limit for Si fracture (~150 nm for spheres,[16] ~300 nm for wires[91]). Break-in of the anode is expected to sufficiently occur during the formation cycles.

All optimization has been performed using the MATLAB curve fitting toolbox.[92] The full optimization problem is stated below:

Q_1: CC capacity exchanged before voltage hold

Q_{hold}^{final}: Total capacity exchanged during voltage hold

Q_2: CC capacity exchanged after voltage hold

Q_{hys}: Apparent capacity fade due to kinetic, transport limitations

Find a, c, Q_{hys} with $p = 0.5$ such that Eqs. 1–2, 4–5 or 1–2, 6, 7) are satisfied. If $p = 0.5$ does not accurately fit the data, p can be varied.

Fitting parameter bounds:

a: (0, 5)

c: (0, 100)

p: (0.3, 1)

Q_{hys}: (0, $Q_{ch,5}$–$Q_{dis,5}$)Here, $Q_{ch,5}$is the charge capacity and $Q_{dis,5}$ is the discharge capacity in the 5th cycle (cycle after V-hold). Q_{hys} is required when considering the CC portion of the discharge after hold because silicon anodes can show high impedance, and large diffusivity variation between charge and discharge causing large differences in charge vs discharge capacity that is not purely due to SEI. Typically, we attribute all coulombic inefficiency between slow rate CC charge and discharge to parasitic SEI capacity. In silicon anode systems, not all the coulombic inefficiency is related to parasitic SEI growth. Some of it can be attributed to finite rate effects in Si causing an apparent capacity fade between charge and discharge. Q_{hys} can be different in the hold vs diagnostic cycles. In a conditioned cell, the values should be similar as Q_{hys} is related to material properties, SEI and stress states which should not vary significantly between subsequent cycles.

The algorithm of computing the optimal fit is given in detail below:

1. Extract Q_{hold}^{final}, $Q_1$and $Q_2$from voltage hold data.
2. Vary $Q_{hys}$from 0 to $Q_{ch,5}$-$Q_{dis,5}$ in 0.1% increments
3. Calculate Q_{rev}^{final} and Q_{irrev}^{final} from Eqs. 4–7.
4. Find (a, p) pairs satisfying $Q_{irrev}^{final} = at_{final}^{p}$.
5. Use a value corresponding to $p = 0.5$ and c as a fitting parameter to fit entire timeseries Q_{hold} data. Compute goodness of fit. If $R^2 \sim 0.999$, this is the optimal fit.
6. If $p = 0.5$, $Q_{hys} = 0$ does not produce best fit, maximize R^2 by varying Q_{hys}, p.

Results and Discussion

Figure 2 shows the electrochemical performance of the LiBOB (top) vs $LiPF_6$ (bottom) cell during the first and second cycle. Figures 2a–2c correspond to the cell voltage, cathode potential vs Li and anode potential vs Li respectively for the LiBOB cell. Corresponding results for the $LiPF_6$ cell are shown in Figs. 2d–2f. In the inset figures of (a), (c), (d), (e) are magnified versions of the first charge cell voltage and anode potential plateau regions corresponding to the dominant SEI decomposition reaction pathways. Note S4 (Figs. S7–S8) shows the incremental capacity analysis of cycles 1–2 with both electrolytes. Upon assembly, pristine LiBOB and $LiPF_6$ cells lie at 0.35 V and 0.39 V respectively; cells are charged up to 4.1 V during 1st lithiation with subsequent discharge to 3.0 V. For the LiBOB cell, a 1st cycle plateau occurs at 1.9 V full cell voltage with anode potential at 1.75 V. Figure S7 shows the LiBOB cell dQ/dV analysis where we can observe peaks associated with these potentials on the first charge. This is attributable to LiBOB salt reduction at the negative electrode as the dominant SEI formation pathway. Literature suggests that LiBOB decomposes at around 1.7 to 1.75 V vs Li/Li^+ and is known to from a thin and stable SEI.[93] An alternative decomposition pathway in the LiBOB electrolyte is decomposition of ethylene carbonate solvent (EC) to lithium alkyl carbonates (LEDC) and ethylene gas with decomposition potential lying around 0.8 V vs Li/Li^+.[74] Hence, we can accurately assign the anode potential plateau at ~1.75 V to decomposition of the LiBOB salt. Capacity loss from SEI formation is mainly from the 1st cycle; a coulombic efficiency of 74.6% observed for cycle 1 with an increase to 96.3% observed in the 2nd cycle. During cell cycling between 3–4.1 V for cycle 2, the positive potential changes between 3.68–4.2 V while the negative potential changes between 0.68–0.1 V. For the $LiPF_6$ cell, FEC reduction at the negative electrode occurs at ~2.6 V cell voltage corresponding to ~1.1 V anode potential. We also see the first peak in the $LiPF_6$ cell incremental capacity analysis in Fig. S8 at these potentials. In literature, FEC reduction potentials have been reported around 0.9 V.[43] Again, capacity loss from SEI formation is mainly from the 1st cycle. A coulombic efficiency of 77.9% is observed for cycle 1 while 2nd cycle efficiency is bumped up to 96.0%. During cell cycling between 3–4.1 V for cycle 2, the positive potential changes between 3.67–4.19 V while the negative potential changes from between 0.67–0.09 V. It is evident that the anode reaches ~100 mV at top of charge for both LiBOB and $LiPF_6$ electrolytes.

Figure 3 compares impedance data for the unfluorinated vs fluorinated electrolyte systems using hybrid pulse power characterization (HPPC) test and electrochemical impedance spectroscopy (EIS). Figures 3a–3c shows the full cell, cathode, and anode area-specific impedances (ASIs) as a function of full cell voltage, cathode potential, and anode potential respectively from the HPPC test. Higher full cell impedance is observed for the LiBOB electrolyte vs $LiPF_6$ electrolyte. This higher impedance stems primarily from the negative electrode (see Fig. 3c) with a smaller contribution arising from the positive electrode (see Fig. 3b). LiBOB anode shows nearly double the area specific impedance of $LiPF_6$ anode (~35 Ω cm^2 vs 20 Ω cm^2). Consequently, it can be hypothesized that LiBOB decomposition results in the formation of more resistive products at the Si|Gr surface as compared to $LiPF_6$ electrolyte; while electrolyte decomposition at the NMC532 cathode forms similar resistivity magnitude products for both salt systems. This data corroborates the observations of Hernandez et al. who have previously demonstrated higher interfacial resistances of the LiBOB system as compared to $LiPF_6$ system during cycling.[94]

EIS data (see Figs. 3d–3f) collected at a full cell voltage of 3.7 V corroborates the higher Li^+ charge transfer resistance in the LiBOB system as compared to $LiPF_6$. Again, the reference electrode setup allows for the deconvolution of full cell impedance (see Fig. 3d) to its positive (see Fig. 3e) and negative electrode contributions (see Fig. 3f). Two semicircles are observable in the impedance data accounting for film resistance and intercalation/alloying charge transfer resistance with a more pronounced double arc feature observable in the cathode. Cathode impedance is higher for LiBOB cell as compared to $LiPF_6$, as evidenced by the larger semicircles, but a more pronounced difference is again observed in anode impedance; the semicircle spans from 5–20 Ω cm^2 on the real axis for LiBOB as compared to 4–6 Ω cm^2 for $LiPF_6$. The wider mid-frequency arc in negative LiBOB impedance can be attributed to greater resistance to Li^+ motion in the SEI. The longer "Warburg tail" suggests greater diffusional impedance (in electrolyte within electrode pores and through the particles).

Figures 4a, 4b shows the cathode and anode potential profiles for the two electrolytes during the voltage hold cycle with specific focus on the hold portion. Full cell voltage, cathode, anode potentials during the entire hold cycle is shown in Fig. S9 (Note S5). For the LiBOB electrolyte, the positive potential increases from 4.21 to 4.23 V, while the negative potential increases from 0.11 to 0.13 V during the 472 h full cell V-hold at 4.1 V. The anode and cathode potential upwards slippage during the hold occurs simultaneously to maintain a constant full cell voltage. The concurrent rise in potential indicates simultaneous decrease in lithiation state of both anode and cathode; open circuit potentials for graphite,[73] Si[72] and NMC532[6] show a decreasing trend with increase in lithiation. The situation is a bit complicated for Si|Gr blends as lithium inventory exchange can also occur between the silicon and graphite anodes during the V-hold resulting in the observed potential rise.[95] Nearly 10 mV of the 20 mV increase in anode, cathode potential with LiBOB electrolyte is during the first ten hours of the hold indicating higher magnitudes of reversible, irreversible currents during the initial phase of the V-hold. With the relaxation of concentration and potential gradients within the electrodes during the latter phase of the CV step, the system reaches an equilibrium where most of the potential rise can be attributed to SEI formation. It is to be noted that the rise of anode and cathode potentials is observed during cycle aging of NMC532-Si|Gr cells between a fixed voltage window as well due to the recurring loss of Li ions as they become incorporated into the SEI of the Si–Gr negative electrode.[28,96]

For the $LiPF_6$ electrolyte, we see a similar rise in anode and cathode potentials as well. The positive potential increases from 4.23

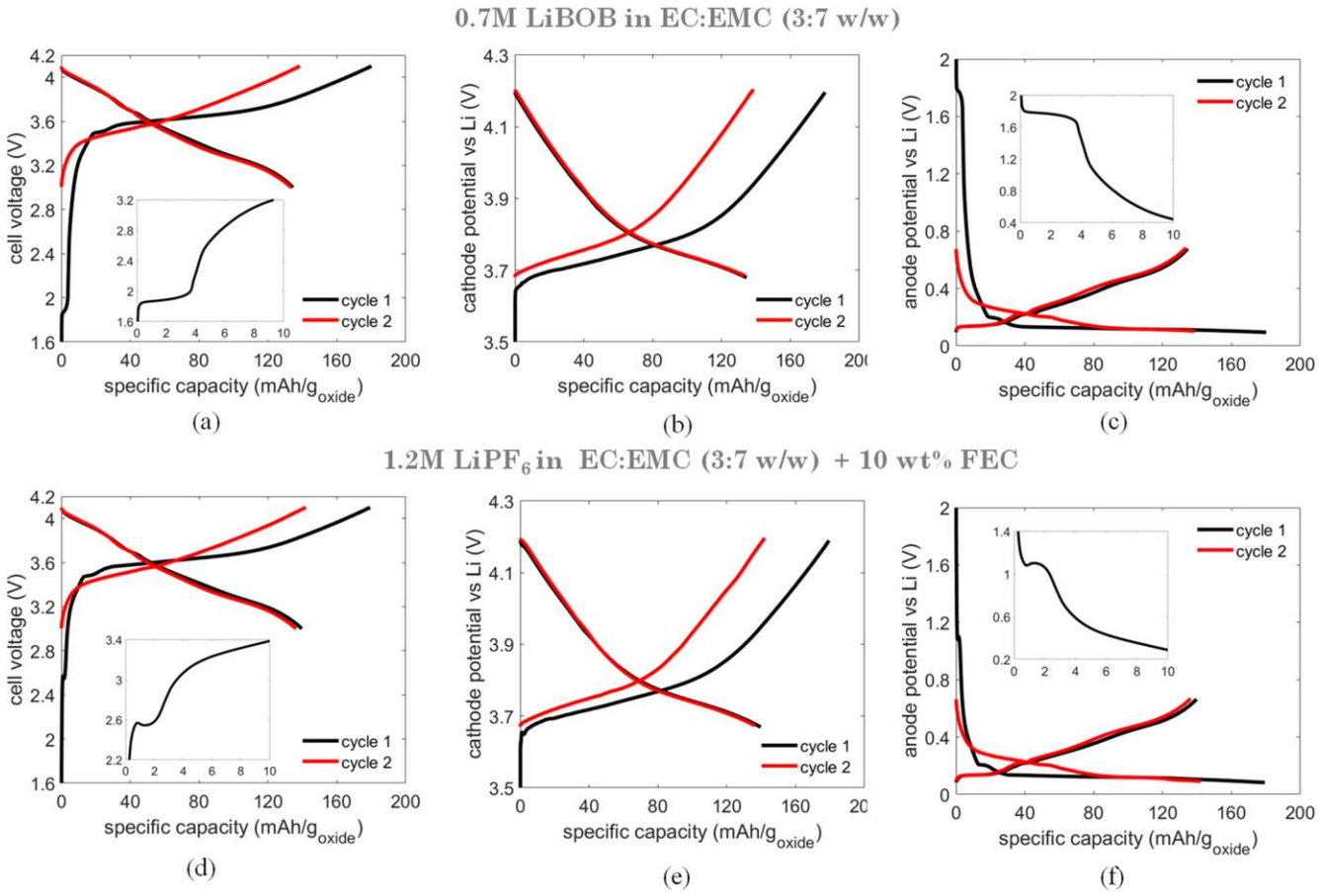

Figure 2. (a) Cell voltage, (b) cathode potential and (c) anode potential for unfluorinated electrolyte system 0.7 M LiBOB in EC:EMC (3:7 w/w) during first two formation cycles. (d) Cell voltage, (e) cathode potential and (f) anode potential for fluorinated electrolyte system 1.2 M $LiPF_6$ in EC:EMC (3:7 w/w) + 10 wt% FEC during first two formation cycles. Inset figures in (a), (c), (d) and (f) show the zoomed voltage and anode potential profiles where plateaus exist.

to 4.25 V while the negative potential increases from 0.13 to 0.15 V during the 600 h full cell V-hold at 4.2 V. Approximately, 12 mV of this 20 mV increase is during the first ten hours of the hold; again, equilibration of concentration, potential gradients on the particle, electrode scale combined with kinetic overpotentials and SEI growth plateauing results in a slower, steady potential rise in the latter half of the hold.

Figures 5a–5c shows the temporal evolution of experimental (symbols) and model (line) capacity and current data during the V-holds for LiBOB and $LiPF_6$ electrolyte. Capacity, currents are normalized with the nominal discharge capacity before the hold (cycle 3) to enable standardized comparison across the two electrolyte systems. A normalized capacity rise of 11.32% vs 8.33% is observed for the LiBOB vs $LiPF_6$ electrolytes during the 472 and 600 h of hold respectively. Fit statistics are listed in Table II. Parameters with 95% confidence intervals are provided for both free and constrained model. Fully constrained model is used as our optimal model. LiBOB hold capacity shows a good match with $p = 0.5$ with low residuals (see Fig. S10). Figures S11 and S12 show the capacity fits and residual for $LiPF_6$ electrolyte with $p = 0.69$ and $p = 0.5$ respectively. It is evident that $p = 0.5$ does not provide the best fit for this system; consequently, p is varied until the fit residuals are minimized with a high R^2. The LiBOB system takes a non-zero value for the hysteresis capacity (1.0%) while the $LiPF_6$ system shows negligible hysteresis (0.2%). This points to more acute kinetics and transport limitations in charge vs discharge for the LiBOB cell compared to $LiPF_6$. Higher LiBOB cell impedance indicates a more resistive SEI and is hypothesized to be the rationale for this observation.

The impact of relaxing capacity constraints (Eqs. 3–6) and considering zero hysteresis capacity on the fits is also analyzed. Note S6 and Figs. S10–S12 show the fits with considerations of all constraints (Eqs. 1–7) and finite capacity hysteresis ($Q_{hys} \neq 0$). This includes all relevant physics while providing a goodness of fit $R^2 \sim 0.998$ and has been considered as our optimal model. Note S7 and Figs. S13, S14 show the hold capacity fits without considering capacities before and after the hold, zero Q_{hys} and $p = 0.5$. Fits show $R^2 \sim 0.999$ for LiBOB, $R^2 \sim 0.989$ for $LiPF_6$ in this scenario with low residuals as there are fewer constraints on the model parameters with incomplete physics. Even with this optimization without constraints, the $LiPF_6$ cell shows higher residuals with $p = 0.5$ indicating the need for a different exponent. Note S8 and Figs. S15, S16 show the fits with consideration of the capacities before, after the hold (Eqs. 1–6) with $Q_{hys} = 0$ and $p = 0.5$. low residuals for LiBOB is observed with $R^2 \sim 0.993$, while $LiPF_6$ shows a relatively poor fit ($R^2 \sim 0.952$). This stems from the need for a different exponent than $p = 0.5$ for $LiPF_6$. The rationale for including Q_{hys} in the final model is also evident from this exercise as R^2 increases to 0.998 with Q_{hys}.

Experimental current during V-hold data in Figs. 5b, 5c and corresponding model fits also show a good match. LiBOB cells shows a lower scatter in the current data as compared to the $LiPF_6$ cell, with normalized current magnitudes ranging between 10^{-3} to 10^{-5} h^{-1} for a major portion of the hold for both systems. Deconvolution of the hold capacity into reversible and irreversible contributions reveals higher proportion of reversible capacities for the LiBOB electrolyte as compared to the $LiPF_6$ electrolyte (5.62% vs 2.48%) while the irreversible capacity proportions for the two electrolytes are similar (5.70% vs 5.85%) (see Fig. 5d). Based on

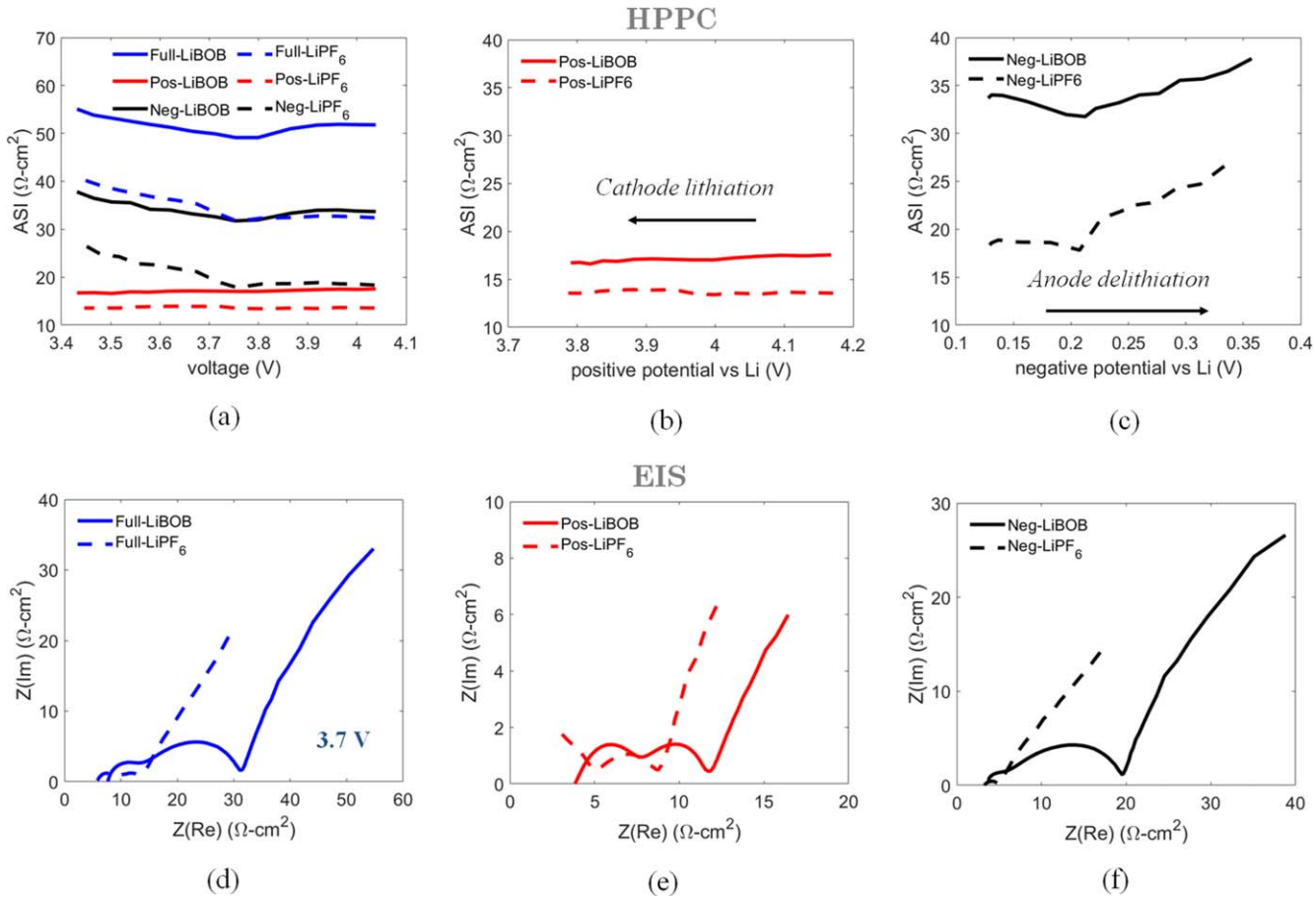

Figure 3. Variation of area specific impedance (ASI) with (a) full cell voltage, (b) cathode potential and (c) anode potential for non-fluorinated (0.7 M LiBOB in EC:EMC (3:7 w/w)) and fluorinated (1.2 M LiPF6 in EC:EMC (3:7 w/w) + 10 wt % FEC) electrolyte systems obtained using hybrid pulse power characterization tests with 10 s, C discharge pulse. Impedance spectrum of (c) full cell, (d) cathode and (e) anode for non-fluorinated (0.7 M LiBOB in EC:EMC (3:7 w/w)) and fluorinated (1.2 M LiPF6 in EC:EMC (3:7 w/w) + 10 wt % FEC) electrolyte systems obtained using electrochemical impedance spectroscopy.

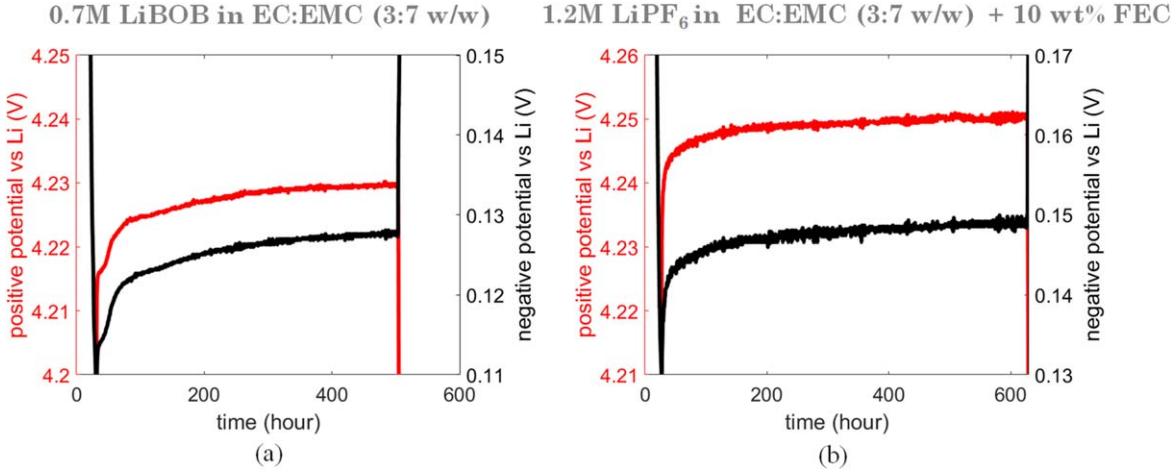

Figure 4. Cathode and anode potential profiles during the voltage hold for (a) LiBOB and (b) $LiPF_6$ electrolyte.

irreversible capacity magnitudes during the hold, the two electrolytes perform similarly for calendar life. Herein lies the importance of accurate hold capacity deconvolution to its parasitic counterpart to glean quantitative calendar life information. It is inaccurate to directly take the hold capacity to be synonymous with parasitic capacity growth due to LLI to the SEI. Looking at just the hold capacity magnitudes, the LiBOB electrolyte shows significantly higher capacity exchanged during the hold as compared to $LiPF_6$ electrolyte (11.32% vs 8.33%) which can be erroneously construed as $LiPF_6$ electrolyte being better for calendar life than LiBOB if we assign all that capacity to irreversible SEI growth. However, it is noteworthy that there is significant reversible lithiation happening during the V-hold that needs to be accounted for prior to getting parasitic capacity estimates. With our deconvolution algorithm, tracking reversible and irreversible capacities accurately is possible

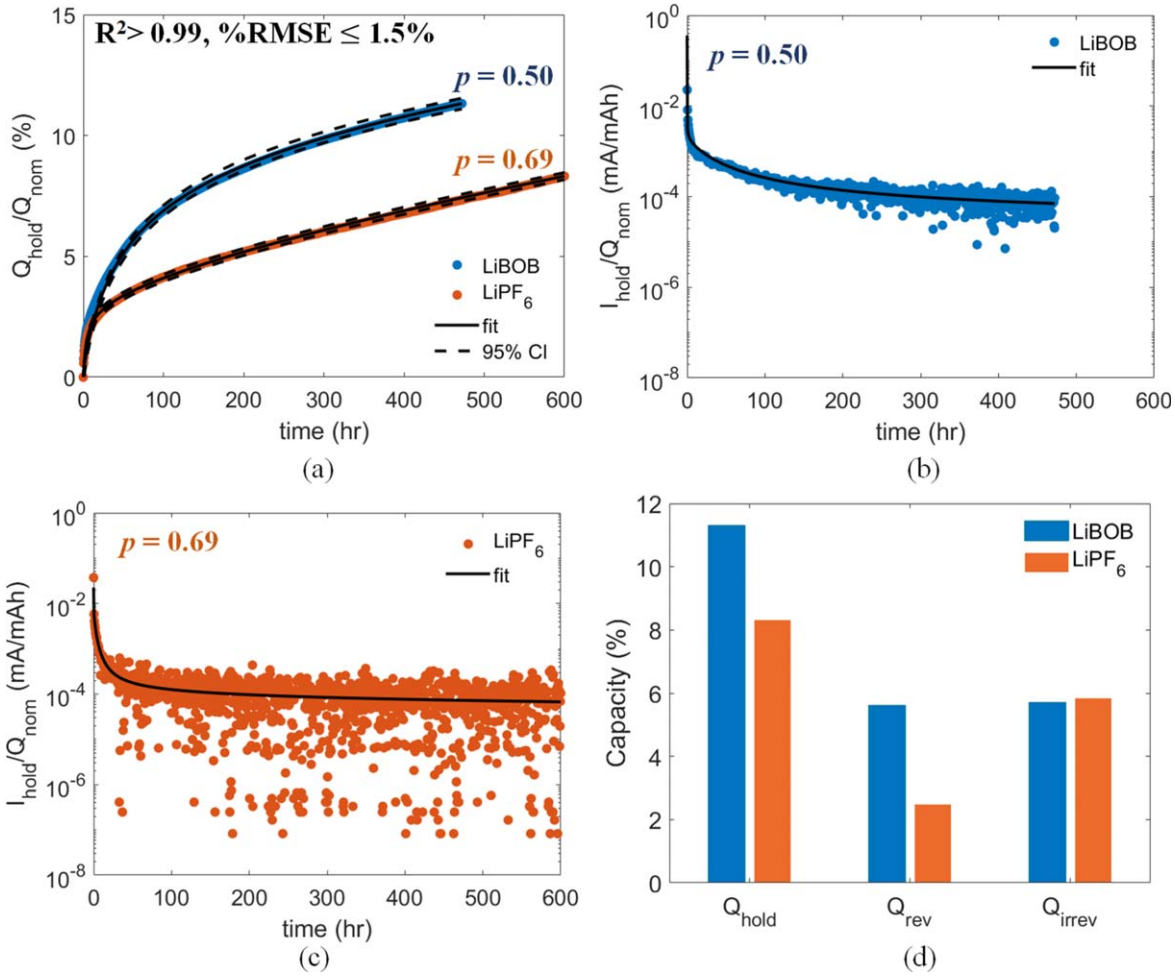

Figure 5. (a) Normalized experimental capacity rise during voltage-hold for LiBOB and $LiPF_6$ electrolytes with model fit. (b–c) Experimental current during voltage-hold with model fit for (b) LiBOB electrolyte and (c) $LiPF_6$ electrolyte. (d) Experimental hold capacity and deconvoluted reversible, irreversible capacity plots for LiBOB and $LiPF_6$ electrolytes.

Table II. Fit Statistics.

	Optimal model without constraints		Optimal model with all constraints	
	LiBOB	$LiPF_6$	LiBOB	$LiPF_6$
a	0.4384 (0.4354, 0.4415)	0.00356 (0.00344, 0.00375)	0.26240	0.07076
p	0.458 (0.457, 0.459)	1.1 (1.094, 1.106)	0.50	0.69
c	28.6 (28.51, 28.69)	22.4 (22.2, 22.61)	44.24 (43.84, 44.65)	3.80 (3.65, 3.95)
Q_{rev}^{final} (%)	1.80	4.24	5.62	2.48
Q_{hys}(%)	—	—	1.0	0.2
SSE (sum of squares due to error)	0.03457	0.4149	7.7470	6.7197
R^2 (goodness of fit)	1	0.9999	0.9984	0.9979
RMSE (root mean square error)	0.006055	0.01861	0.09054	0.0748

leading to meaningful quantitative calendar lifetime estimates for rapid electrolyte screening.

We can also compare the calendar lifetime of the two electrolytes by extrapolating the irreversible capacity trend to the future beyond the voltage hold duration where the cell reaches 20% capacity fade (see Fig. 6). Extrapolating the irreversible parasitic capacity growth rate to estimate the time for which the cell capacity will reach 80% of its nominal value, we see that the LiBOB electrolyte shows a calendar lifetime of ∼240 days (8 months) while the $LiPF_6$ electrolyte lasts for ∼150 days (5 months). The capacity progression and normalized lifetime estimates are shown in Fig. 5e with the $LiPF_6$ electrolyte performing ∼40% inferior to the LiBOB system. It should be noted that $LiPF_6$ has shorter calendar life (∼30% inferior) even if we neglect the impact of higher capacity hysteresis in LiBOB (see Fig. S17). Quantitative lifetime predictions lie well below calendar lives of commercial state of the art graphite cells (∼15 years). The rationale for such a result is three-fold: firstly, commercial cells undergo an extensive formation and conditioning procedure that can last on the order of 3–4 weeks on a highly optimized electrode, electrolyte and cell design with huge expense on R&D and standardized manufacturing lines,[97,98] while this is a lab-made unoptimized silicon containing cell. Secondly, the V-hold

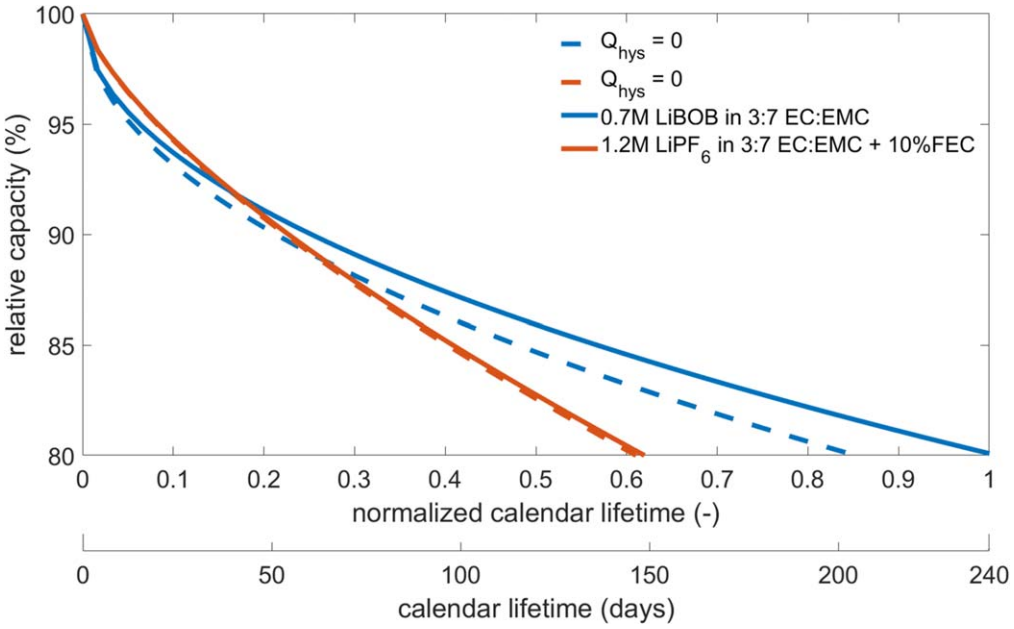

Figure 6. Calendar lifetime predictions for LiBOB vs $LiPF_6$ electrolyte from model extrapolation with and without hysteresis.

protocol subjects the cell to an accelerated degradation pathway with the constant V-hold as compared to the traditional USABC OCV-RPT protocol where the cell is subject to milder open circuit voltage conditions.[35] The exacerbated capacity loss leads to more conservative lifetime estimates from V-hold as compared to if the same cell were subject to the OCV-RPT protocol. Thirdly, the V-hold can conflate reversible and irreversible self-discharge processes which can make the irreversible capacity numbers higher.[35] Consequently, it is advisable to use the V-hold protocol with the capacity deconvolution algorithm in a semi-quantitative fashion for such purposes as shown here e.g. rapid material screening for better calendar life.

Figures 7a–7b shows the voltage vs specific capacity during charge and discharge for cycles before (cycle 3) and after the hold (cycle 5) for LiBOB electrolyte and $LiPF_6$ electrolyte respectively. LiBOB cell shows good discharge capacity retention from cycle 3 to cycle 5 ($\sim$132 mAh g^{-1} in both cycles) while $LiPF_6$ cell has a drop in discharge capacity from 135 mAh g^{-1} to 122 mAh g^{-1}. This is also an indication of lowered Li inventory remaining in the $LiPF_6$ cell from losses to the SEI. Consequently, the diagnostic CC cycles after the hold contain important electrochemical signatures of the reversible and irreversible lithiation before the hold.

Finally, we attempt to shed light on the physical processes causing potentiostatic hold aging characteristics to deviate from open circuit rest aging behavior. Figures 8a–8c encompasses a visualization of differences in the electrochemical phenomena occurring at the cell and particle levels for aging under OCV rest vs V-hold. A full gamut of electrode level processes that can occur in the cell is highlighted in Fig. 8a. External circuit is closed during V-hold and open during OCV rest. During normal CCCV charging,

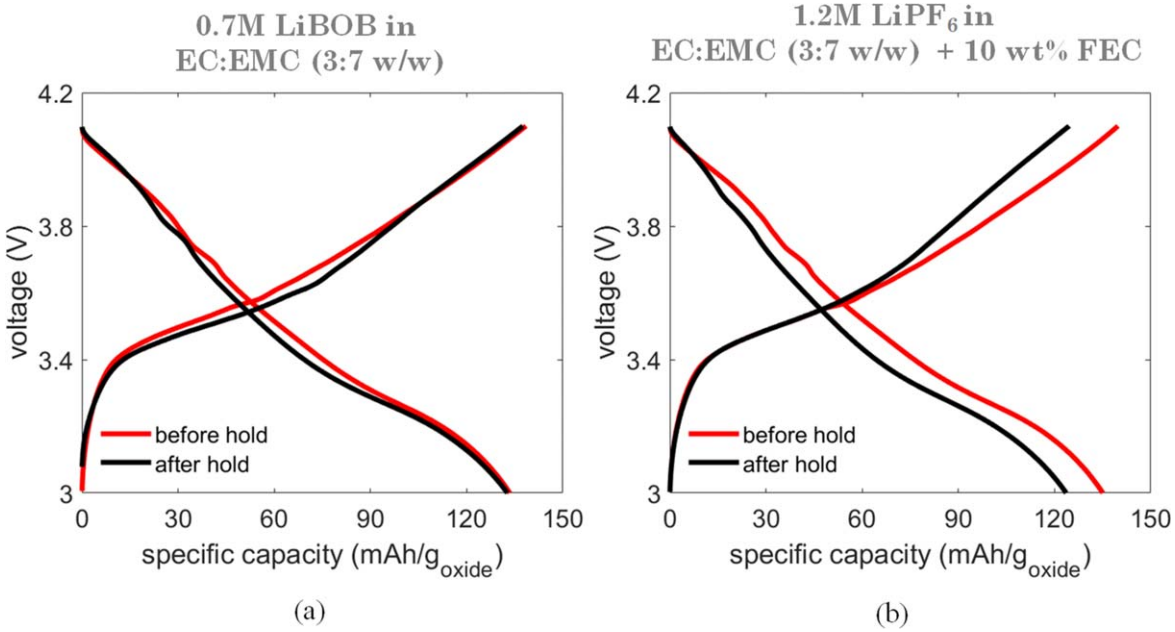

Figure 7. Performance curves (voltage vs specific capacity) during charge and discharge for cycles before and after voltage hold for (a) LiBOB electrolyte and (b) $LiPF_6$ electrolyte.

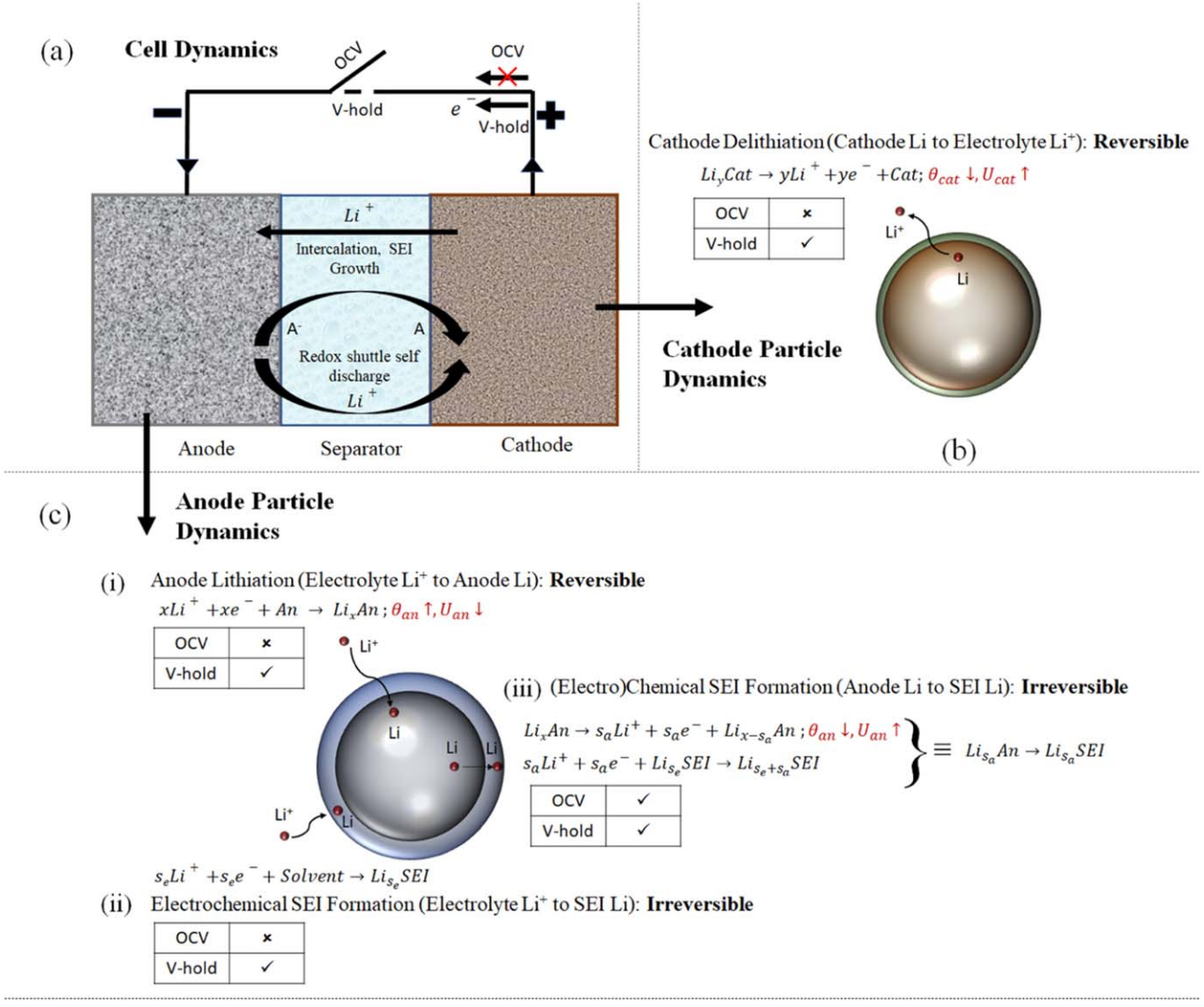

Figure 8. Visualization of electrochemical processes occurring at the (a) cell level, (b) cathode particle and (c) anode particle for voltage hold vs open circuit voltage rest. Anode dynamics can include (i) anode lithiation, (ii) electrochemical SEI formation from cathode Li to electrolyte Li^+ to anode SEI Li and (iii) (electro)chemical SEI formation from anode Li to anode SEI Li.

lithium ions (Li^+) and electrons (e^-) can flow from the cathode to the anode through the electrolyte and external circuit respectively. This Li^+ can be involved in reversible anode lithiation or parasitic solvent reduction to SEI components like LEDC, LiF etc. As V-hold is akin to CV charging, closed-loop external and internal circuits allow for simultaneous transfer of e^- and Li^+ delithiated from the cathode towards the anode, while this electrochemical route is shut off during the OCV rest because of the open loop. Simultaneously, reversible self-discharge via redox shuttles can occur at the anode allowing for Li^+ and anionic solvent species (A^-) to flow and combine at the cathode.[99] This can be a feature during OCV-RPT as well as V-hold, but is slow at low temperatures and low states of charge.[100] During initial portion of the V-hold, downhill electrolyte gradients (salt concentration, potential) are set up from cathode to anode requiring uphill diffusion and migration of Li^+ from anode to cathode for self-discharge.

Particle level dynamics for the cathode and anode are described in detail in Figs. 8b, 8c respectively. Each particle is represented by a sphere with a film on top meant to represent the cathode and anode electrolyte interphases (CEI, SEI) respectively. Note, that CEI dynamics are typically much weaker compared to the SEI formation on the anode, consequently, this is represented by a smaller film thickness for the cathode particle in the schematic. During V-hold, cathode delithiates releasing Li^+ into the electrolyte resulting in a decrease in cathode Li stoichiometry, θ_{cat}, and an increase in the cathode potential, U_{cat} (for cathodes with sloping open circuit potential profile like NMC). This is observed in our three-electrode cells as well with the creeping up of NMC cathode potential during the hold with both electrolytes. During OCV rest, this process will not occur due to unavailability of an electron transfer route and the cathode potential remains relatively constant.

The anode particle dynamics has three distinct processes outlined (see Figs. 8c–8i, 8ii, 8iii). (i) During V-hold, the delithiated Li^+ from the cathode moves through the electrolyte to the anode and can get reversibly intercalated into the anode. This results in an increase in anode Li stoichiometry, θ_{an}, and a corresponding decrease in anode potential, U_{an} (for typical graphite, silicon anodes with sloping open circuit profile). (ii) Alternatively, this electrolyte Li^+ and corresponding electron released from the cathode to the anode can reduce the solvents and be irreversibly lost in forming the anode SEI. Since this process does not involve the reduced Li in the anode, it does not lead to a change in stoichiometry or potential of the anode, though it registers as current through the external circuit. (iii) Finally, reduced Li present in the anode can chemically/

electrochemically decompose the solvents to form the anode SEI. This process results in reduction of anode Li stoichiometry, θ_{an}, and a corresponding increase in anode potential, U_{an}. While all the three processes are active during V-hold, it is only the third process that takes centerstage during OCV rest. So, during OCV rest, the anode loses Li continuously to the SEI resulting in anode potential rise and overall cell voltage decay. For V-hold, reversible anode lithiation (i) and irreversible Li loss from the anode (iii) to the anode SEI are two opposing factors for anode stoichiometry change. Creeping up of anode potential in our three-electrode cells during voltage holds indicates overall lithium loss due to net delithiation of the anode from the combination of all three processes. This is a consequence of the cycler maintaining constant full cell voltage conditions during the hold as an increase in cathode potential needs to be compensated by a corresponding increase in anode potential.

Limitations

Here, the V-hold protocol was applied to a Si-Gr|NMC532 cell with N:P ~1 where both the cathode and anode have sloped potential profiles. The V-hold protocol is best applied to a cathode with flat voltage profile like lithium-iron phosphate (LFP) which maintains constant anode and cathode potentials during the hold when we apply a fixed cell voltage. This allows for a more standardized calendar life comparison across material systems with equivalent anode state of charge.[35] Furthermore, the optimal N:P ratio for V-hold tests is suggested to be $<<1$ with the excess Li inventory allowing for the direct applicability of Eq. 3; limited Li inventory scenario makes the deconvolution cumbersome.[35] In this study, the three-electrode setup can track the negative potentials directly; this provides additional electrochemical data to perform the deconvolution accurately and have a standardized comparison between the two electrolyte systems. Anode potential in the two systems lie 20 mV apart during the V-hold which is hypothesized to be insignificant to cause any drastic change in the results as compared to the scenario where anode potentials in both systems were equal. Another relevant consideration is that, when the V-hold occurs at a state of charge in which the slope of the voltage profile of the cathode is comparable to that of the anode (as is the case here, see Figs. S18b–S18c), the measured currents carries mixed information from both oxidation and reduction side reactions.[35] Consequently, the use of cathodes with sloped voltage profiles can affect attempts to extrapolate calendar lifetimes from these experiments.

Recently, Rodrigues has demonstrated that the smoother nature of the sloped potential profile of Si towards end of delithiation can obscure the cycling coulombic inefficiencies through additional capacity access as compared to the steeper potential profile for Gr towards end of delithiation.[90] Here, the anode is 15% Si—73% Gr blend, as opposed to pure Gr, consequently we will have finite impact of this reservoir effect with NMC cathode. Note S10 and Fig. S18 show the incremental capacity profiles for the two electrolyte systems investigated here during the constant current portions of the voltage hold cycle. Quantification of excess capacity access requires dQ/dV magnitudes from Si-Gr half-cell data on the anode potentials being accessed in this system. Figure S18c plots the dQ/dV vs anode potential with similar magnitudes observed for both LiBOB and $LiPF_6$ cell. Consequently, we can presume the reservoir effect to affect both the cells in a similar fashion. This limitation can be further relaxed by using LFP cathode with flat voltage profile for any subsequent V-hold studies.

The capacity fits are more sensitive to the choice of exponent p which can have a significant impact on the choice of parameter c. Ideally, if different material systems yield a similar value of p and show similar SEI resistances, the parameter c can be directly attributed to the diffusion, kinetic limitations in the anode active material, SEI and be used for comparing active material performance alongside SEI performance; a high value of c indicates sluggish plateauing of reversible lithiation indicating more transport, charge transfer limitations in the active material and SEI. A physics-based approach with coupled electrochemistry-transport-mechanics model that can track the reversible lithiation in the anode with potentiostatic holds may add more accuracy to the deconvolution; albeit with much higher complexity requiring good thermodynamic, kinetic, diffusive property estimates.[101]

Conclusions and Outlook

This study utilized reference electrode cells under a potentiostatic hold protocol to evaluate the impact of fluorination on calendar life of blended Si–Gr anode|NMC532 cells. The V-hold protocol subjects the cell to both reversible lithiation and irreversible SEI growth processes during charge, consequently, an accurate deconvolution algorithm is devised to ascertain the parasitic capacity losses to the SEI. The irreversible capacity trends are further extrapolated to generate insights into the calendar life; here, LiBOB electrolyte in EC:EMC (3:7 w/w) outperforms $LiPF_6$ electrolyte in EC:EMC (3:7 w/w) + 10 wt% FEC. The novel V-hold protocol has been studied as a potential tool for high throughput materials and cell screening for calendar life as compared to the benchmark standard OCV-RPT protocol which is slow but provides quantitative estimates.[35] In this study, we provide the know-how for splitting the hold capacity into its irreversible component to get semiquantitative estimates for calendar life.

Our approach can be utilized towards finding novel electrolytes for high Si anodes. The approach, in principle, is extensible to other anode systems e.g. Li metal. Also, the semi-quantitative nature allows for making statements like "Y electrolyte is n times better than X electrolyte." Consequently, if we run OCV-RPT tests on X electrolyte giving an actual quantitative lifetime of t_X years, we can make a prediction of the actual quantitative lifetime of the Y electrolyte to be $n \times t_X$ years. Here, the caveats lie in the sudden change of degradation trajectory due to capacity knees (e.g electrolyte dryout)[102] which cannot be captured in the V-hold because it's essentially early life testing. The testing and analysis approach can reduce the experimental, labor costs of running long OCV-RPT tests on new electrolyte systems for calendar life estimation significantly. Identification of potential electrolytes meeting calendar life goals is possible in ~2 months of potentiostatic hold testing once a cell with baseline electrolyte has undergone the OCV-RPT protocol to end of life.

Acknowledgments

This research was supported by the U.S. Department of Energy's Vehicle Technologies Office under the Silicon Consortium Project, directed by Brian Cunningham, and managed by Anthony Burrell. This manuscript was created by the Alliance for Sustainable Energy, LLC, the manager, and operator of the National Renewable Energy Laboratory for the U.S. Department of Energy (DOE) under Contract No. DE-AC36–08GO28308. This work was authored in part by UChicago Argonne, LLC, Operator of Argonne National Laboratory ("Argonne"). Argonne, a U.S. Department of Energy Office of Science laboratory, is operated under Contract No. DE-AC02–06CH11357. The views expressed in the article do not necessarily represent the views of the DOE or the U.S. Government. The U.S. Government retains and the publisher, by accepting the article for publication, acknowledges that the U.S. Government retains a nonexclusive, paid-up, irrevocable, worldwide license to publish or reproduce the published form of this work, or allow others to do so, for U.S. Government purposes.

ORCID

Ankit Verma https://orcid.org/0000-0002-7610-8574
Maxwell C. Schulze https://orcid.org/0000-0001-8368-4054
Andrew Colclasure https://orcid.org/0000-0002-9574-5106
Marco-Tulio Fonseca Rodrigues https://orcid.org/0000-0003-0833-6556

Stephen E Trask https://orcid.org/0000-0002-0879-4779
Krzysztof Pupek https://orcid.org/0009-0006-9094-5340
Christopher S. Johnson https://orcid.org/0000-0003-4357-6889
Daniel P. Abraham https://orcid.org/0000-0003-0402-9620

References

1. M. Armand and J.-M. Tarascon, *Nature*, **451**, 652 (2008).
2. E. J. Cairns and P. Albertus, *Annual Review of Chemical and Biomolecular Engineering*, **1**, 299 (2010).
3. M. Li, J. Lu, Z. Chen, and K. Amine, *Adv. Mater.*, **30**, 1800561 (2018).
4. B. Nykvist and M. Nilsson, *Nat. Clim. Change*, **5**, 329 (2015).
5. Y. Xia, J. Zheng, C. Wang, and M. Gu, *J. Nano Energy*, **49**, 434 (2018).
6. A. Verma, K. Smith, S. Santhanagopalan, D. Abraham, K. P. Yao, and P. P. Mukherjee, *J. Electrochem. Soc.*, **164**, A3380 (2017).
7. J. E. Harlow, X. Ma, J. Li, E. Logan, Y. Liu, N. Zhang, L. Ma, S. L. Glazier, M. M. Cormier, and M. Genovese, *J. Electrochem. Soc.*, **166**, A3031 (2019).
8. B. Liang, Y. Liu, and Y. Xu, *J. Power Sources*, **267**, 469 (2014).
9. B. Liu, J.-G. Zhang, and W. Xu, *Joule*, **2**, 833 (2018).
10. J. Sturm, A. Rheinfeld, I. Zilberman, F. B. Spingler, S. Kosch, F. Frie, and A. Jossen, *J. Power Sources*, **412**, 204 (2019).
11. C.-H. Chen et al., *J. Electrochem. Soc.*, **167**, 080534 (2020).
12. A. Zülke, I. Korotkin, J. M. Foster, M. Nagarathinam, H. Hoster, and G. Richardson, *J. Electrochem. Soc.*, **168**, 120522 (2021).
13. A. Verma and P. P. Mukherjee, *J. Electrochem. Soc.*, **164**, A3570 (2017).
14. D. E. Galvez-Aranda, A. Verma, K. Hankins, J. M. Seminario, P. P. Mukherjee, and P. B. Balbuena, *J. Power Sources*, **419**, 208 (2019).
15. S. W. Lee, M. T. McDowell, L. A. Berla, W. D. Nix, and Y. Cui, *Proc. Natl Acad. Sci.*, **109**, 4080 (2012).
16. X. H. Liu, L. Zhong, S. Huang, S. X. Mao, T. Zhu, and J. Y. Huang, *ACS Nano*, **6**, 1522 (2012).
17. C. K. Chan, H. Peng, G. Liu, K. McIlwrath, X. F. Zhang, R. A. Huggins, and Y. Cui, *Nat. Nanotechnol.*, **3**, 31 (2008).
18. M. Kummer, J. Badillo, A. Schmitz, H.-G. Bremes, M. Winter, C. Schulz, and H. Wiggers, *J. Electrochem. Soc.*, **161**, A40 (2013).
19. N. Liu, H. Wu, M. T. McDowell, Y. Yao, C. Wang, and Y. Cui, *Nano Lett.*, **12**, 3315 (2012).
20. S. Hy, Y.-H. Chen, H.-M. Cheng, C.-J. Pan, J.-H. Cheng, J. Rick, and B.-J. Hwang, *ACS Applied Materials*, **7**, 13801 (2015).
21. J. Shin, T.-H. Kim, Y. Lee, and E. Cho, *Energy Storage Mater.*, **25**, 764 (2020).
22. Y. Sun, J. Lopez, H. W. Lee, N. Liu, G. Zheng, C. L. Wu, J. Sun, W. Liu, J. W. Chung, and Z. Bao, *J Advanced Materials*, **28**, 2455 (2016).
23. J. D. McBrayer, M.-T. F. Rodrigues, M. C. Schulze, D. P. Abraham, C. A. Apblett, I. Bloom, G. M. Carroll, A. M. Colclasure, C. Fang, and K. L. Harrison, *Nat. Energy*, **6**, 866 (2021).
24. M. Dubarry, N. Qin, and P. Brooker, *Current Opinion in Electrochemistry*, **9**, 106 (2018).
25. P. Keil, S. F. Schuster, J. Wilhelm, J. Travi, A. Hauser, R. C. Karl, and A. Jossen, *J. Electrochem. Soc.*, **163**, A1872 (2016).
26. M. Montaru, S. Fiette, J.-L. Koné, and Y. Bultel, *Journal of Energy Storage*, **51**, 104544 (2022).
27. W. Lu, L. Zhang, Y. Qin, and A. Jansen, *J. Electrochem. Soc.*, **165**, A2179 (2018).
28. K. Kalaga, M.-T. F. Rodrigues, S. E. Trask, I. A. Shkrob, and D. P. Abraham, *Electrochim. Acta*, **280**, 221 (2018).
29. I. Zilberman, S. Ludwig, and A. Jossen, *Journal of Energy Storage*, **26**, 100900 (2019).
30. I. Zilberman, J. Sturm, and A. Jossen, *J. Power Sources*, **425**, 217 (2019).
31. J. P. Christophersen, *Battery Test Manual For Electric Vehicles, revision 3,* (Idaho National Lab.(INL), Idaho Falls, ID (United States)) (2015).
32. M. Naumann, M. Schimpe, P. Keil, H. C. Hesse, and A. Jossen, *Journal of Energy Storage*, **17**, 153 (2018).
33. M.-T. F. Rodrigues, Z. Yang, S. E. Trask, A. R. Dunlop, M. Kim, F. Dogan, B. Key, I. Bloom, D. P. Abraham, and A. N. Jansen, *J. Power Sources*, **565**, 232894 (2023).
34. P. Gasper, K. Gering, E. Dufek, and K. Smith, *J. Electrochem. Soc.*, **168**, 020502 (2021).
35. M. C. Schulze, M.-T. F. Rodrigues, J. D. McBrayer, D. P. Abraham, C. A. Apblett, I. Bloom, Z. Chen, A. M. Colclasure, A. R. Dunlop, and C. Fang, *J. Electrochem. Soc.*, **169**, 050531 (2022).
36. Y. S. Meng, V. Srinivasan, and K. Xu, *Science*, **378**, eabq3750 (2022).
37. H. B. Son, M.-Y. Jeong, J.-G. Han, K. Kim, K. H. Kim, K.-M. Jeong, and N.-S. Choi, *J. Power Sources*, **400**, 147 (2018).
38. M. T. Ong, O. Verners, E. W. Draeger, A. C. Van Duin, V. Lordi, and J. E. Pask, *J. Phys. Chem. B*, **119**, 1535 (2015).
39. K. Fulfer and D. Kuroda, *Phys. Chem. Chem. Phys.*, **19**, 25140 (2017).
40. S. Han, *Sci. Rep.*, **9**, 1 (2019).
41. X. Fan, L. Chen, O. Borodin, X. Ji, J. Chen, S. Hou, T. Deng, J. Zheng, C. Yang, and S.-C. Liou, *Nat. Nanotechnol.*, **13**, 715 (2018).
42. N. Yao, X. Chen, X. Shen, R. Zhang, Z. H. Fu, X. X. Ma, X. Q. Zhang, B. Q. Li, and Q. Zhang, *Angew. Chem.*, **133**, 21643 (2021).
43. T. Hou, G. Yang, N. N. Rajput, J. Self, S.-W. Park, J. Nanda, and K. A. Persson, *Nano Energy*, **64**, 103881 (2019).
44. R. Jung, M. Metzger, D. Haering, S. Solchenbach, C. Marino, N. Tsiouvaras, C. Stinner, and H. A. Gasteiger, *J. Electrochem. Soc.*, **163**, A1705 (2016).
45. I. A. Shkrob, J. F. Wishart, and D. P. Abraham, *J. Phys. Chem. C*, **119**, 14954 (2015).
46. X. Chen, X. Li, D. Mei, J. Feng, M. Y. Hu, J. Hu, M. Engelhard, J. Zheng, W. Xu, and J. Xiao, *ChemSusChem*, **7**, 549 (2014).
47. Y. Ha, D. P. Finegan, A. M. Colclasure, S. E. Trask, and M. Keyser, *J Electrochimica Acta*, **394**, 139097 (2021).
48. Y. Ha, C. Stetson, S. P. Harvey, G. Teeter, B. J. Tremolet de Villers, C.-S. Jiang, M. Schnabel, P. Stradins, A. Burrell, and S.-D. Han, *ACS Applied Materials*, **12**, 49563 (2020).
49. J. Burns, N. Sinha, G. Jain, H. Ye, C. M. VanElzen, E. Scott, A. Xiao, W. Lamanna, and J. Dahn, *J. Electrochem. Soc.*, **160**, A2281 (2013).
50. S. Wiemers-Meyer, S. Jeremias, M. Winter, and S. Nowak, *J Electrochimica Acta*, **222**, 1267 (2016).
51. K. Xu, S. Zhang, T. R. Jow, W. Xu, and C. A. Angell, *Electrochemical Solid-State Letters*, **5**, A26 (2001).
52. K. Xu, U. Lee, S. Zhang, M. Wood, and T. R. Jow, *Electrochemical Solid-State Letters*, **6**, A144 (2003).
53. K. Xu, U. Lee, S. Zhang, J. L. Allen, and T. R. Jow, *Electrochemical Solid-State Letters*, **7**, A273 (2004).
54. K. Xu, U. Lee, S. S. Zhang, and T. R. Jow, *J. Electrochem. Soc.*, **151**, A2106 (2004).
55. K. Xu, S. Zhang, and R. Jow, *J. Power Sources*, **143**, 197 (2005).
56. K. Xu, S. Zhang, and T. R. Jow, *Electrochemical Solid-State Letters*, **8**, A365 (2005).
57. K. Xu, S. S. Zhang, U. Lee, J. L. Allen, and T. R. Jow, *J. Power Sources*, **146**, 79 (2005).
58. S.-Y. Ha, J.-G. Han, Y.-M. Song, M.-J. Chun, S.-I. Han, W.-C. Shin, and N.-S. Choi, *J Electrochimica Acta*, **104**, 170 (2013).
59. M. Xu, L. Zhou, Y. Dong, Y. Chen, A. Garsuch, and B. L. Lucht, *J. Electrochem. Soc.*, **160**, A2005 (2013).
60. Y. Wang, L. Xing, X. Tang, X. Li, W. Li, B. Li, W. Huang, H. Zhou, and X. Li, *RSC Adv.*, **4**, 33301 (2014).
61. S. Kranz, T. Kranz, A. G. Jaegermann, and B. Roling, *J. Power Sources*, **418**, 138 (2019).
62. B. Lu, Y. Song, Q. Zhang, J. Pan, Y.-T. Cheng, and J. Zhang, *Phys. Chem. Chem. Phys.*, **18**, 4721 (2016).
63. V. A. Sethuraman, V. Srinivasan, A. F. Bower, and P. R. Guduru, *J. Electrochem. Soc.*, **157**, A1253 (2010).
64. W. Dreyer, J. Jamnik, C. Guhlke, R. Huth, J. Moškon, and M. Gaberšček, *Nat. Mater.*, **9**, 448 (2010).
65. Y. Jiang, G. Offer, J. Jiang, M. Marinescu, and H. Wang, *J. Electrochem. Soc.*, **167**, 130533 (2020).
66. M. Ganser, F. E. Hildebrand, M. Klinsmann, M. Hanauer, M. Kamlah, and R. M. McMeeking, *J. Electrochem. Soc.*, **166**, H167 (2019).
67. J. Christensen and J. Newman, *J. Solid State Electrochem.*, **10**, 293 (2006).
68. M. J. Chon, V. A. Sethuraman, A. McCormick, V. Srinivasan, and P. R. Guduru, *Phys. Rev. Lett.*, **107**, 045503 (2011).
69. K. Higa and V. Srinivasan, *J. Electrochem. Soc.*, **162**, A1111 (2015).
70. W. Mai, A. Colclasure, and K. Smith, *J. Electrochem. Soc.*, **166**, A1330 (2019).
71. N. Ding, J. Xu, Y. Yao, G. Wegner, X. Fang, C. Chen, and I. Lieberwirth, *Solid State Ionics*, **180**, 222 (2009).
72. R. Chandrasekaran, A. Magasinski, G. Yushin, and T. F. Fuller, *J. Electrochem. Soc.*, **157**, A1139 (2010).
73. Y. Ji, Y. Zhang, and C.-Y. Wang, *J. Electrochem. Soc.*, **160**, A636 (2013).
74. P. Lu, C. Li, E. W. Schneider, and S. J. Harris, *J. Phys. Chem. C*, **118**, 896 (2014).
75. X. Zhang, R. Kostecki, T. J. Richardson, J. K. Pugh, and P. N. Ross, *J. Electrochem. Soc.*, **148**, A1341 (2001).
76. Q. Li, Z. Cao, W. Wahyudi, G. Liu, G.-T. Park, L. Cavallo, T. D. Anthopoulos, L. Wang, Y.-K. Sun, and H. N. Alshareef, *ACS Energy Lett.*, **6**, 69 (2020).
77. S. K. Heiskanen, J. Kim, and B. L. Lucht, *Joule*, **3**, 2322 (2019).
78. A. L. Michan, B. S. Parimalam, M. Leskes, R. N. Kerber, T. Yoon, C. P. Grey, and B. L. Lucht, *Chem. Mater.*, **28**, 8149 (2016).
79. Y. Jin, N.-J. H. Kneusels, L. E. Marbella, E. Castillo-Martínez, P. C. Magusin, R. S. Weatherup, E. Jónsson, T. Liu, S. Paul, and C. P. Grey, *JACS*, **140**, 9854 (2018).
80. A. B. Gunnarsdóttir, S. Vema, S. Menkin, L. E. Marbella, and C. P. Grey, *J. Mater. Chem. A*, **8**, 14975 (2020).
81. M. Stich, M. Göttlinger, M. Kurniawan, U. Schmidt, and A. Bund, *J. Phys. Chem. C*, **122**, 8836 (2018).
82. E. W. C. Spotte-Smith, T. B. Petrocelli, H. D. Patel, S. M. Blau, and K. A. Persson, *ACS Energy Lett.*, **8**, 347 (2022).
83. P. M. Attia, W. C. Chueh, and S. J. Harris, *J. Electrochem. Soc.*, **167**, 090535 (2020).
84. F. Single, A. Latz, and B. Horstmann, *ChemSusChem*, **11**, 1950 (2018).
85. L. von Kolzenberg, A. Latz, and B. Horstmann, *ChemSusChem*, **13**, 3901 (2020).
86. F. Single, B. Horstmann, and A. Latz, *J. Electrochem. Soc.*, **164**, E3132 (2017).
87. G. M. Veith, M. Doucet, J. K. Baldwin, R. L. Sacci, T. M. Fears, Y. Wang, and J. F. Browning, *J. Phys. Chem. C.*, **119**, 20339 (2015).
88. G. M. Veith, M. Doucet, R. L. Sacci, B. Vacaliuc, J. K. Baldwin, and J. F. Browning, *Sci. Rep.*, **7**, 1 (2017).
89. I. Hasa, A. M. Haregewoin, L. Zhang, W.-Y. Tsai, J. Guo, G. M. Veith, P. N. Ross, and R. Kostecki, *ACS Applied Materials*, **12**, 40879 (2020).
90. M.-T. F. Rodrigues, *J. Electrochem. Soc.*, **169**, 110514 (2022).
91. I. Ryu, J. W. Choi, Y. Cui, and W. D. Nix, *J. Mech. Phys. Solids*, **59**, 1717 (2011).
92. The MathWorks Inc. MATLAB version: 9.10.0.1669831 (R2021a), Natick, Massachusetts: The MathWorks Inc. https://mathworks.com (2021).

93. J.-C. Panitz, U. Wietelmann, M. Wachtler, S. Ströbele, and M. Wohlfahrt-Mehrens, *J. Power Sources*, **153**, 396 (2006).
94. G. Hernández, A. J. Naylor, Y.-C. Chien, D. Brandell, J. Mindemark, and K. Edström, *ACS Sustainable Chemistry*, **8**, 10041 (2020).
95. D. J. Pereira, A. M. Aleman, J. W. Weidner, and T. R. Garrick, *J. Electrochem. Soc.*, **169**, 020577 (2022).
96. M. Luo, M.-T. F. Rodrigues, L. L. Shaw, and D. P. Abraham, *ACS Appl. Energy Mater.*, **5**(5), 5513 (2022).
97. Y. Liu, R. Zhang, J. Wang, and Y. Wang, *IScience*, **24**, 102332 (2021).
98. P. A. Nelson, S. Ahmed, K. G. Gallagher, and D. W. Dees, *Modeling The Performance And Cost Of Lithium-Ion Batteries For Electric-Drive Vehicles* (in, Argonne National Lab.(ANL), Argonne, IL (United States)) (2019).
99. D. Lu, M. S. Trimboli, Y. Wang, and G. L. Plett, *J. Electrochem. Soc.*, **169**, 120515 (2022).
100. S. Büchele, E. Logan, T. Boulanger, S. Azam, A. Eldesoky, W. Song, M. Johnson, and M. Metzger, *J. Electrochem. Soc.*, **170**, 010518 (2023).
101. J. Li, F. Yang, X. Xiao, M. W. Verbrugge, and Y.-T. Cheng, *J Electrochimica Acta*, **75**, 56 (2012).
102. P. M. Attia, A. Bills, F. B. Planella, P. Dechent, G. Dos Reis, M. Dubarry, P. Gasper, R. Gilchrist, S. Greenbank, and D. Howey, *J. Electrochem. Soc.*, **169**, 060517 (2022).